Performance Analysis of a Flux-Concentrating Field-Modulated Permanent-Magnet Machine for Direct-Drive Applications

Xianglin Li[1], Kwok tong Chau[2], *Fellow, IEEE*, Ming Cheng[1], *Fellow, IEEE*, Byungtaek Kim[3], and Robert D. Lorenz[4], *Fellow, IEEE*

[1]School of Electrical Engineering, Southeast University, Nanjing 210096, China
[2]Department of Electrical and Electronic Engineering, University of Hong Kong, Hong Kong
[3]Department of Electrical Engineering, Kunsan University, Gunsan 573-701, Korea
[4]Department of Mechanical Engineering, University of Wisconsin—Madison, Madison, WI 53706 USA

This paper presents a field-modulated permanent magnet (FMPM) machine using spoke-magnet-array outer rotor for direct-drive applications. The operating principle with detailed theoretical derivation is analyzed to reveal the evidence for high torque capability of the proposed machine, just due to the utilization of effective harmonic flux adding to the contribution of air-gap fundamental flux for energy conversion. Using the finite element analysis, the performance characteristics of the proposed machine are assessed and compared with permanent magnet synchronous machine counterparts to verify the theoretical analysis. A prototype machine is also fabricated for experimental validation of the proposed machine. The analytical discussions also form an important foundation for research in various high-performance FMPM machines.

***Index Terms*—Direct drive, field-modulated machine, flux concentrating, permanent-magnet machine, spoke magnet.**

NOMENCLATURE

$B_{\rm ag}$	Air-gap flux density.
$B_{{\rm ag}c}$	Effective air-gap flux density in permanent-magnet synchronous machine (PMSM).
$B_{{\rm ag}h}$	Higher order components of $B_{\rm ag}$.
$B_{{\rm ag}v}$	Effective air-gap flux density in field-modulated permanent magnet (FMPM) machine.
B_r	Remanence of permanent magents (PMs).
$e_{{\rm ph}c}$	Phase electromotive force (EMF) of PMSM.
$e_{{\rm ph}v}$	Phase EMF of FMPM machine.
$E_{\rm ph}$	Amplitude of phase EMF.
$E_{{\rm ph}c}$	Amplitude of $e_{{\rm ph}c}$.
$E_{{\rm ph}v}$	Amplitude of $e_{{\rm ph}v}$.
$E_{\rm RMS}$	Root mean square (RMS) value of phase EMF.
$F_{\rm ag}$	Equivalent air-gap magnetomotive force (MMF).
$F_{{\rm ag}j}$	Amplitude of jth component of $F_{\rm ag}$.
F_m	MMF of one pole of rotor PMs.
$F_{{\rm ag}m}$	MMF of one pole of equivalent air-gap.
G_r	Speed ratio.
$h_{\rm sy}$	Thickness of stator yoke.
h_t	Depth of stator slot.
$I_{\rm ph}$	Amplitude of phase current.
$I_{\rm RMS}$	RMS value of phase current.
j	Integers equal to 1, 3, 5,…,+∞.
J_s	Slot current density.
k	Integers equal to 1, 2, 3,…,+∞.
k_c	Carter's coefficient.
k_{d1}	Effective fundamental distribution factor of phase windings.
$k_{\rm df}$	Flux leakage factor in flux-concentrating FMPM (FCFMPM) machine.
l_m	Radial length of rotor PMs.
L_a	Stack length.
m	Number of phases.
n_r	Mechanical speed of rotor.
$N_{\rm cog}$	Least common multiple between rotor pole number and stator tooth number.
$N_{\rm ph}$	Number of turns per phase windings.
$N_{\rm st}$	Number of stator teeth.
p_r	Number of PM pole pairs on rotor.
p_s	Number of pole-pairs of stator armature windings.
q	Number of slots per pole of armature windings.
r_g	Average radius of physical air gap.
$R_{g'}$	Reluctance of equivalent air-gap with angular width $\theta_p/2$.
R_m	Reluctance of one pole of rotor PMs.
T_e	Electromagnetic torque.
$T_{\rm ec}$	Electromagnetic torque of PMSM.
$T_{\rm ev}$	Electromagnetic torque of FMPM machine.
μ_0	Vacuum permeability.
$\mu_{\rm rm}$	Relative permeability of PMs.
ω_r	Angular velocity of rotor.
ω_s	Angular velocity of air-gap flux harmonic in FMPM machine.
$\delta_{\rm cog}$	Mechanical angle period of cogging torque.
δ_g	Physical air-gap length.
$\delta_{g'}$	Equivalent air-gap length equal to $k_c\delta_g$.
θ	Circumferential position.
θ_m	Angular width of one pole of rotor PMs.
θ_p	Angular width of one pole of rotor iron.
θ_s	Angular width of stator slot.
θ_t	Angular width of stator tooth.
θ_τ	Slot pitch.
Λ	Air-gap permeance.
Λ_0	Average value of Λ.
Λ_k	Amplitude of kth component of Λ.
Λ_t	Permeance of stator tooth and corresponding air gap.

Manuscript received August 31, 2014; revised November 3, 2014; accepted November 13, 2014. Date of publication November 26, 2014; date of current version May 22, 2015. Corresponding author: M. Cheng (e-mail: mcheng@seu.edu.cn).

Color versions of one or more of the figures in this paper are available online at http://ieeexplore.ieee.org.

Digital Object Identifier 10.1109/TMAG.2014.2374553

Λ_s Permeance of stator slot and corresponding air gap.
σ Coil span.
Φ_m Flux per pole of rotor PMs.
ψ_{ph} Phase PM flux linkage.

I. Introduction

LOW-SPEED PM machines are increasingly drawing significant attention in direct-drive applications, such as wind power generation [1], electric vehicles [2], [3], and so on. A comparison with the gearbox-driven counterparts showed that the direct-drive PM machines have several attractive merits of compact structure, light weight, and high efficiency [4]. The multipole PMSM as a direct-drive solution has been extensively developed and studied [5]. In [6], the new material-efficient axial pole pairing technique for cogging torque and torque ripple reductions in direct-drive machines was also demonstrated. To generate reluctance torque, a direct-drive PMSM with soft magnetic composite interpoles was proposed and analyzed in [7]. Moreover, the dual mechanical port machine has also attracted great attention due to its prospect in wind turbine and hybrid electric vehicle applications as a continuous variable transmission [8], [9]. It can be seen that although the pole–slot configuration and overall construction are different, all aforementioned direct-drive machines always rely on the fundamental component of electromagnetic field to realize electromechanical energy conversion.

Recently, the magnetic gearing effect derived from the coaxial magnetic gear (CMG) [10], [11] has become more and more attractive when designing low-speed direct-drive PM vernier (PMV) machines [12]. In [13], a dual-stator spoke-array PMV machine was also developed to obtain high power factor and significantly high torque capability. Moreover, a high-speed outer rotor PM machine has been directly integrated inside the CMG to constitute a composite magnetic-geared PM (MGPM) machine for low-speed direct-drive application [14], [15], which shows a high torque density but desires a complex structure involving two rotating bodies and three air gaps. Then, its simplified version, namely, a two-air-gap MGPM machine, was proposed and analyzed in [16]. In [17], the one-air-gap MGPM machine was also achieved by directly equipping flux-modulation poles on the stator. In [18], a quantitative comparison among these three viable MGPM machines was conducted and the results show that the one-air-gap MGPM machine is the most viable for direct-drive applications due to its high torque capability and simple structure. The research also reveals that the one-air-gap MGPM machine is essentially in principle the same as PMV machines. Hence, according to the same operating principle, namely, field modulation principle, both of them can be termed as FMPM machine in general.

In these FMPM machines, the pole-pairs of stator armature windings are configured equal to that of the air-gap effective harmonic flux rather than the fundamental flux to achieve high-speed armature field design while keeping the rotor low-speed rotation. The previous literature mainly focuses on proposing individual structure and making finite element analysis (FEA) [19], [20]. The available literature has all shown that the FMPM machine can provide a higher torque capability than PMSM counterparts [21], [22]; however, the key mechanism of the FMPM machines with high torque density has not been clearly revealed in theory.

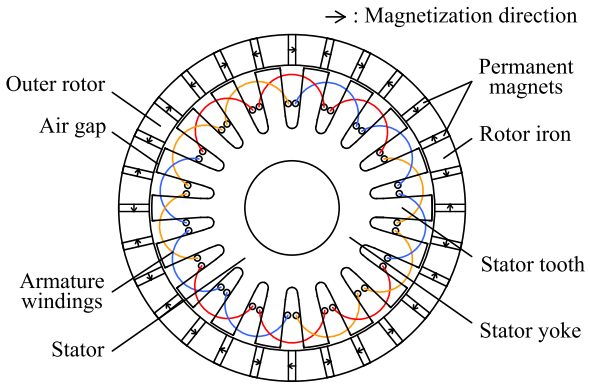

Fig. 1. Configuration of the proposed machine.

The objective of this paper is to present the detailed theoretical derivation based on a newly proposed FCFMPM machine [23], so as to reveal the basic mechanism of high torque density of the PMV machines. Of course, the presented FCFMPM machine in this paper exactly has the same principle with PMV machines, which employs an open-slot stator and a spoke-magnet outer rotor. In the PMV machines, although the stator pole pairs are designed to be equal to that of the effective harmonic flux rather than fundamental flux, both fluxes can be simultaneously used for the torque transmission. It is the additional utilization of effective harmonic flux that causes a torque capability improvement in the PMV machines. In Section II, the configuration of the proposed machine will be presented. Then Section III will focus on the operating principle analysis and theoretically deriving the torque expression to elaborate high torque capability of the proposed machine. The performance comparison and experimental verification will be done in Sections IV and V, respectively. The conclusion will be drawn in Section VI.

II. Machine Configuration

Fig. 1 shows the configuration of the proposed machine [23]. To facilitate direct-drive applications such as for in-wheel motors and wind turbines, the outer-rotor structure is preferable which can also increase the air-gap diameter and hence the torque production. Moreover, a spoke-magnet-array is adopted on the rotor, which is useful for the air-gap flux density improvement and hence the developed torque.

Differing from the PMV machine in [17] that employs a split-pole stator, the proposed machine adopts an open-slot stator. In general, the split-pole stator has two main drawbacks as shown in Fig. 2: 1) some flux lines cannot effectively link with the armature windings, just close through the split poles, which reduce the utilization of the magnetic field and 2) the slots between the split poles become large dead spaces, which reduces the space utilization. Thus, the open-slot stator is

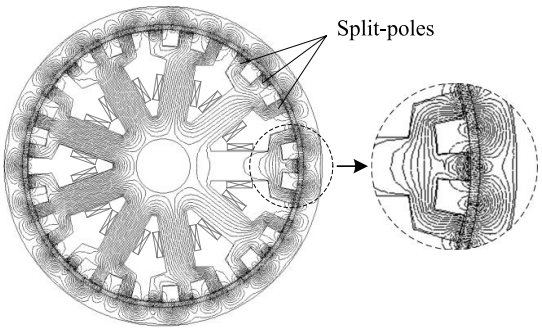

Fig. 2. No-load flux distribution of the split-pole FMPM machine.

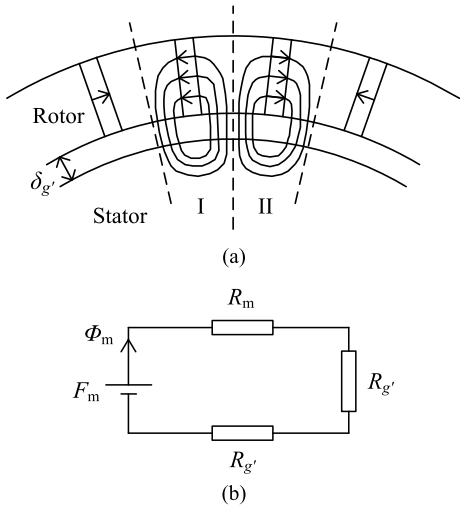

Fig. 3. Flux model and equivalent magnetic circuit for air-gap MMF calculation. (a) Flux model. (b) Equivalent magnetic circuit.

adopted in the proposed machine in which the stator teeth can enable the field modulation instead of split poles. There will be no such dead spaces and more flux lines can link with the armature windings. Hence, it is expected that the torque capability of the proposed machine can be further improved under the same overall volume compared with the split-pole FMPM machine.

III. Operating Principle

A. Air-Gap Flux Density

As well known, the alternation of stator teeth and slots can always arouse the change of air-gap permeance in the circumferential direction. Therefore, the basic principle of the FMPM machine is that the MMF generated by PMs on the rotor can be modulated by the uneven air gap permeance and hence, the desired fast flux variation is resulted. To simplify the theoretical analysis, it is assumed that the magnetic saturation of iron core and flux leakage is negligible.

To simplify analytical calculation, the air-gap MMF expression can be first derived based on equivalent air-gap length $\delta_{g'}$ that considers the variation of stator tooth slot. Fig. 3 shows the flux model and equivalent magnetic circuit for air-gap MMF calculation, while Fig. 4 shows the corresponding analytical model and equivalent air-gap MMF waveform.

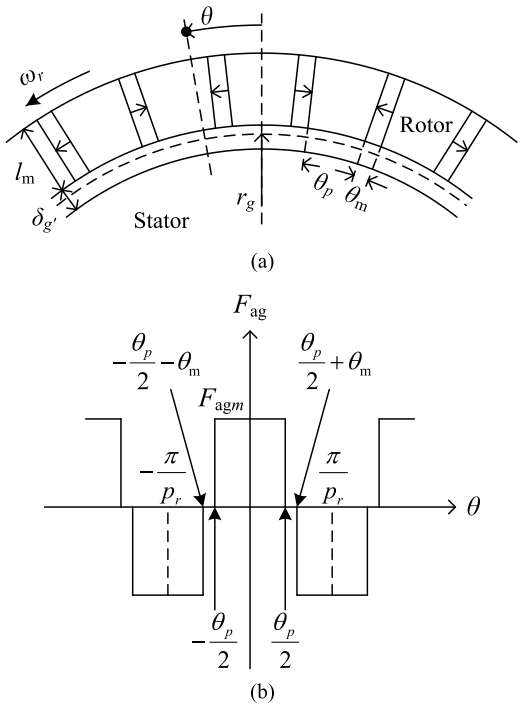

Fig. 4. Analytical model and equivalent waveform for air-gap MMF calculation. (a) Model. (b) Equivalent air-gap MMF waveform.

Based on Fig. 3, the PM flux per pole can be expressed as

$$\Phi_m = \frac{B_r \theta_m \theta_p r_g^2 l_m L_a}{\theta_m \theta_p r_g^2 + 4\delta_{g'} \mu_{rm} l_m}. \tag{1}$$

Therefore, the one-pole air-gap MMF can be calculated as

$$F_{{\rm ag}m} = \frac{2B_r \theta_m r_g l_m \delta_{g'}}{\mu_0 \theta_m \theta_p r_g^2 + 4\mu_0 \mu_{\rm rm} \delta_{g'} l_m}. \tag{2}$$

Based on (2) and the equivalent air-gap MMF waveform shown in Fig. 4(b), considering the rotation of rotor and using discrete Fourier transform, the variation of air-gap MMF with the circumferential position θ can be expressed as

$$F_{\rm ag}(\theta, t) = \sum_{j=1,3}^{+\infty} F_{{\rm ag}j} \cos[j p_r(\theta - \omega_r t)] \tag{3}$$

where the amplitude of the jth component $F_{{\rm ag}j}$ is given by

$$F_{{\rm ag}j} = \frac{4F_{{\rm ag}m}}{j\pi} \sin\left(\frac{j\pi}{2}\right) \cos\left(\frac{j p_r \theta_m}{2}\right). \tag{4}$$

It can be derived that the fundamental amplitude $F_{\rm ag1}$ is greater than zero.

Fig. 5(a) shows the analytical model for air-gap permeance calculation. Considering the alternation of stator teeth and slots, Fig. 5(b) shows the simplified air-gap permeance waveform, in which

$$\Lambda_t = \frac{\mu_0 \theta_t r_g L_a}{\delta_g} \tag{5}$$

$$\Lambda_s = \frac{4\mu_0 L_a}{\pi} \ln\left(1 + \frac{\pi \theta_s r_g}{4\delta_g}\right). \tag{6}$$

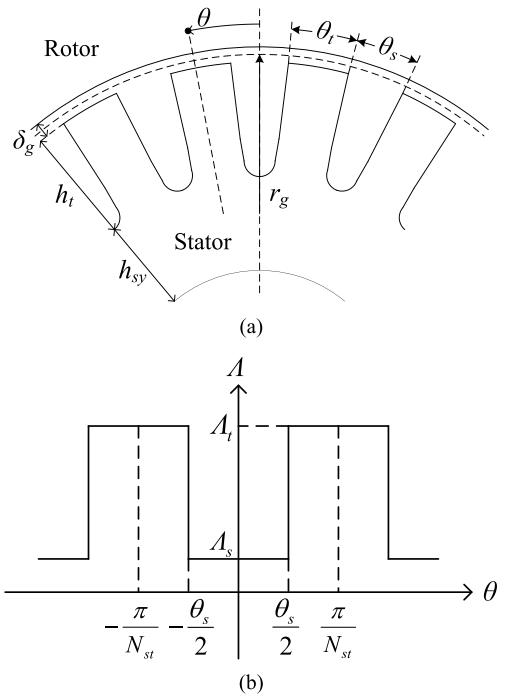

Fig. 5. Analytical model and simplified waveform for air-gap permeance calculation. (a) Model. (b) Simplified air-gap permeance waveform.

Then, using discrete Fourier transform, the variation of air-gap permeance Λ with circumferential position θ can be written in the following form:

$$\Lambda(\theta) = \Lambda_0 + \sum_{k=1,2}^{+\infty} \Lambda_k \cos(kN_{\rm st}\theta) \tag{7}$$

where the coefficients are determined by

$$\Lambda_0 = \frac{N_{\rm st}}{2\pi}(\Lambda_t\theta_t + \Lambda_s\theta_s) \tag{8}$$

$$\Lambda_k = \frac{2(\Lambda_s - \Lambda_t)}{k\pi} \sin\left(\frac{kN_{\rm st}\theta_s}{2}\right). \tag{9}$$

It is obvious that Λ_0 is greater than zero. Also when $k = 1$, due to $\sin(N_{\rm st}\theta_s/2) > 0$, $(\Lambda_s - \Lambda_t) < 0$, so $\Lambda_1 < 0$.

Based on (3) and (7), the air-gap flux density is given by

$$\begin{aligned} B_{\rm ag}(\theta,t) &= \Lambda_0 F_{\rm ag1}\cos[p_r(\theta-\omega_r t)] \\ &+ \frac{\Lambda_1 F_{\rm ag1}}{2}\cos\left[(N_{\rm st}-p_r)\left(\theta - \frac{-p_r}{N_{\rm st}-p_r}\omega_r t\right)\right] \\ &+ \frac{\Lambda_1 F_{\rm ag1}}{2}\cos\left[(N_{\rm st}+p_r)\left(\theta - \frac{p_r}{N_{\rm st}+p_r}\omega_r t\right)\right] + B_{{\rm ag}h} \end{aligned} \tag{10}$$

where $B_{{\rm ag}h}$ represents the high-order harmonics, which can be neglected in the following analytical calculation. It can be seen from (10) that in addition to the fundamental component, there are two large harmonics with the pole-pairs $(N_{\rm st} - p_r)$ and $(N_{\rm st} + p_r)$, respectively. In the PMSMs, the pole-pairs of stator armature windings are always designed to be equal to that of the air-gap fundamental flux, which results that the harmonic fluxes cannot be used for producing electromagnetic torque. That is, the effective air-gap flux density used for torque transmission in the PMSMs can be written as

$$B_{{\rm ag}c}(\theta,t) = \Lambda_0 F_{\rm ag1}\cos[p_r(\theta-\omega_r t)]. \tag{11}$$

However, in the FCFMPM machine, the stator armature windings are wound in accordance with the harmonic flux having the pole pairs $(N_{\rm st} - p_r)$, which can be called as the effective harmonic. In this case, the number of pole pairs in the stator windings satisfies the following:

$$p_s = N_{\rm st} - p_r. \tag{12}$$

An important point to realize here is that not only the fundamental component of air-gap flux contributes to the electromechanical energy conversion, but also this effective harmonic flux can be utilized. Thus, the total effective air-gap flux density used for torque transmission in the FCFMPM machine can be expressed as

$$\begin{aligned} B_{{\rm ag}v}(\theta,t) &= \Lambda_0 F_{\rm ag1}\cos[p_r(\theta-\omega_r t)] \\ &+ \frac{\Lambda_1 F_{\rm ag1}}{2}\cos\left[(N_{\rm st}-p_r)\left(\theta - \frac{-p_r}{N_{\rm st}-p_r}\omega_r t\right)\right]. \end{aligned} \tag{13}$$

From (13), it indicates that the rotational velocity of this effective harmonic flux is governed by

$$\omega_s = -\frac{p_r}{N_{\rm st}-p_r}\omega_r = -G_r\omega_r \tag{14}$$

where G_r is defined as the speed ratio reflecting the magnetic gearing effect of this type of FMPM machines and the minus sign denotes that the rotational direction of this effective harmonic is opposite to the rotor. Although the amplitude of the effective harmonic flux is low, its rotational velocity is G_r times higher than that of the fundamental flux. It is known that fast flux changing can lead to a significant EMF. Thus, the effective harmonic flux can also induce a considerable EMF in stator armature windings. Thus, it is expected that the FMPM machine can exhibit higher torque capability than the PMSM counterparts under the same condition of the air-gap electric and fundamental magnetic loadings due to the contribution of effective harmonic field.

B. Phase EMF

In a three-phase machine, the phase PM flux linkage can be expressed as

$$\psi_{\rm ph}(t) = k_{d1}N_{\rm ph}L_a r_g \int_0^{\sigma\theta_\tau} B_{\rm ag}(\theta,t)d\theta. \tag{15}$$

For the PMSMs, based on (11) and (15), the phase EMF can be deduced as

$$\begin{aligned} e_{{\rm ph}c}(t) &= k_{d1}N_{\rm ph}L_a r_g\omega_r \\ &\times\left[2\Lambda_0 F_{\rm ag1}\sin\left(\frac{\sigma\pi}{2q}\right)\sin\left(p_s\omega_r t - \frac{\sigma\pi}{2q}\right)\right]. \end{aligned} \tag{16}$$

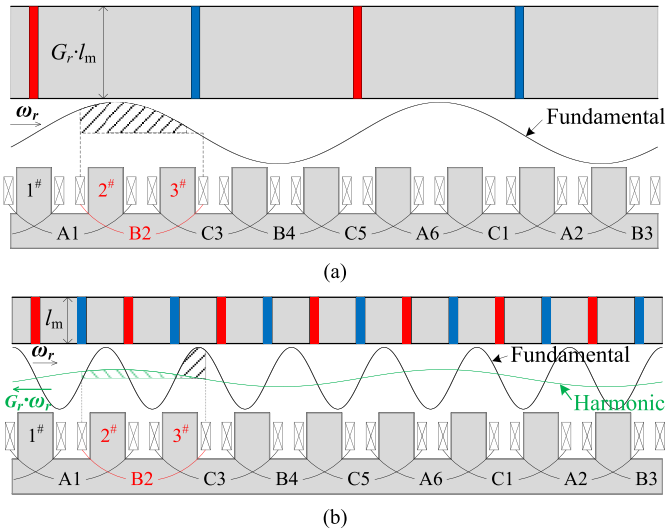

Fig. 6. Schematic of the operating principle. (a) Comparative PMSM counterpart. (b) Proposed 18-slot/8-pole FCFMPM.

On the other hand, based on (13) and (15), the phase EMF in the FCFMPM machine can be expressed as

$$e_{\mathrm{ph}v}(t) = k_{d1} N_{\mathrm{ph}} L_a r_g \omega_r \cdot \left[\begin{array}{l} 2\Lambda_0 F_{\mathrm{ag1}} \sin\left(G_r \dfrac{\sigma\pi}{2q}\right) \sin\left(G_r p_s \omega_r t - G_r \dfrac{\sigma\pi}{2q}\right) \\ +G_r \Lambda_1 F_{\mathrm{ag1}} \sin\left(\dfrac{\sigma\pi}{2q}\right) \sin\left(G_r p_s \omega_r t + \dfrac{\sigma\pi}{2q}\right) \end{array} \right]. \quad (17)$$

It can be seen that the induced EMF by the fundamental and effective harmonic fluxes in the FCFMPM machine have the same electric frequency, and it is G_r times higher than that of the PMSM counterparts. In this paper, an 18-slot/8-pole FCFMPM is set as a case for performance analysis and comparison, in which the number of stator teeth is equal to 18, the PM pole pairs on the rotor is 14, and the pole pairs of stator armature windings is designed as four. Due to the fact that the slot number per pole in this machine is equal to 2.25, a distributed winding with a coil span of two slot pitches is adopted for achieving a large and sinusoidal EMF. Based on (17), the amplitude of phase EMF in this 18-slot/8-pole FCFMPM machine can be deduced as

$$E_{\mathrm{ph}v} = k_{d1} N_{\mathrm{ph}} L_a r_g \omega_r (1.97\Lambda_0 F_{\mathrm{ag1}} - 3.45\Lambda_1 F_{\mathrm{ag1}}). \quad (18)$$

When the same air-gap electric loading and fundamental magnetic loading are applied for a PMSM counterpart having 18 teeth and four PM pole pairs, based on (16), the corresponding phase EMF amplitude can be derived as

$$E_{\mathrm{ph}c} = k_{d1} N_{\mathrm{ph}} L_a r_g \omega_r (1.97\Lambda_0 F_{\mathrm{ag1}}). \quad (19)$$

As mentioned above, $\Lambda_0 > 0$, $\Lambda_1 < 0$, and $F_{\mathrm{ag1}} > 0$, and thus it yields $E_{\mathrm{ph}v} > E_{\mathrm{ph}c}$. It shows that the FCFMPM machine offers improved phase EMF amplitude compared with the PMSMs under the same condition due to the additional utilization of effective harmonic flux. Fig. 6 shows the operating principles of the proposed 18-slot/8-pole FCFMPM and comparative PMSM counterpart. To guarantee the same air-gap fundamental magnetic loading, the length of PMs in the comparative PMSM should be G_r times that of the proposed FCFMPM machine. Under the same rotor speed, stator structure, and electric loading, the air-gap fundamental flux components in both machines can induce the same EMF amplitude, but the effective harmonic flux is additionally utilized for improving the EMF in the proposed FCFMPM machine.

C. Electromagnetic Torque

To evaluate the torque capability, assuming that these analyzed machines are operated as motors and adopting $i_d = 0$ control method, namely, keeping the applied current in phase with the EMF, the transmitted electromagnetic torque can be calculated by

$$T_e = \frac{m E_{\mathrm{ph}} I_{\mathrm{ph}}}{2\omega_r}. \quad (20)$$

Based on (18) and (19), the electromagnetic torque of the proposed 18-slot/8-pole FCFMPM and comparative PMSM can be expressed as

$$T_{\mathrm{ev}} = \frac{m I_{\mathrm{ph}}}{2} k_{d1} N_{\mathrm{ph}} L_a r_g (1.97\Lambda_0 F_{\mathrm{ag1}} - 3.45\Lambda_1 F_{\mathrm{ag1}}) \quad (21)$$

$$T_{\mathrm{ec}} = \frac{m I_{\mathrm{ph}}}{2} k_{d1} N_{\mathrm{ph}} L_a r_g (1.97\Lambda_0 F_{\mathrm{ag1}}) \quad (22)$$

respectively. Thus, due to the same electric loading, namely, the same stator configuration and phase current amplitude I_{ph}, it is supposed that the proposed 18-slot/8-pole FCFMPM is capable of producing higher torque than the comparative PMSM counterpart due to the harmonic flux utilization from the magnetic gearing effect.

IV. Performance Comparison

The FEA is used to investigate performances of the proposed 18-slot/8-pole FCFMPM machine and comparative PMSM counterparts. The electromagnetic characteristics including field distribution, cogging torque, and electromagnetic torque are analyzed and compared in this section. To allow a fair comparison, the air-gap diameter, fundamental magnetic loading, electric loading, and stack length of the analyzed machines are the same. However, due to different operating principles, magnetic field analysis shows that when the same PM volume, namely, fundamental magnetic loading, is applied, the stator iron in the comparative PMSM is very saturated, which will reduce the utilization of PMs and increase the iron losses. Hence, a more reasonable PMSM with reduced amount of PMs (termed as PMSM_2, and the original PMSM is referred as PMSM_1) is also designed and analyzed for convincing comparison. Using the FEA to optimize individual design of analyzed machines, the specifications and key parameters are summarized in Table I.

A. Air-Gap Flux Density

Figs. 7–9 show the no-load air-gap flux density waveforms and their corresponding harmonic spectrum of these

TABLE I
SPECIFICATIONS AND KEY PARAMETERS OF THE THREE ANALYZED MACHINES

Items	FCFMPM	PMSM_1	PMSM_2
Rated speed, n_r [rpm]	214		
Phase no-load EMF, E_{RMS} [V]	228	123	100
Phase current, I_{RMS} [A]	8.33		
No. of rotor pole-pairs, p_r	14	4	
No. of stator teeth, N_{st}	18		
No. of stator pole-pairs, p_s	4		
No. of turns per phase, N_{ph}	162		
Stack length, L_a [mm]	284		
Iron material	DW360-50		
Radial length of PMs, l_m [mm]	20.5	71.75	24.5
Width of PMs, θ_m [rad]	0.039		
Remanence of PMs, B_r [T]	1.15		
Relative permeability of PMs, μ_{rm}	1.07		
Radius of airgap, r_g [mm]	89.25		
Length of airgap, δ_g [mm]	0.5		
Depth of stator slot, h_t [mm]	39		
Thickness of stator yoke, h_{sy} [mm]	20		
Current density, J_s [A/mm^2]	4.15		

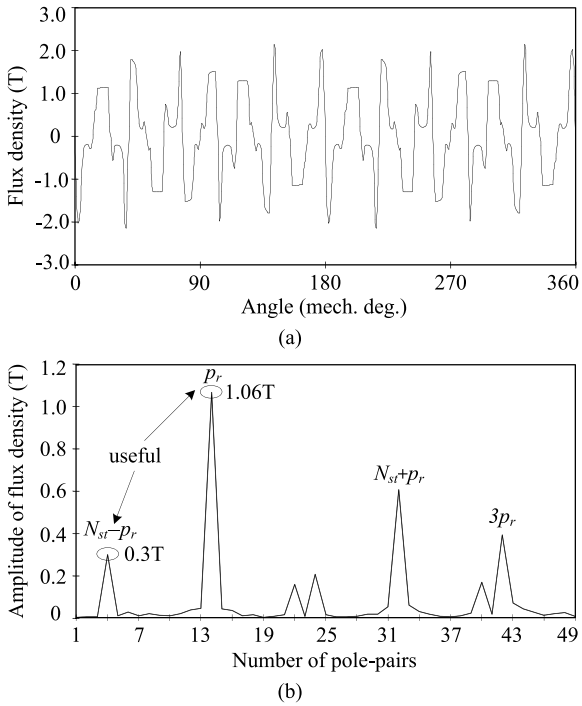

Fig. 7. No-load air-gap flux density of the proposed 18-slot/8-pole FCFMPM. (a) Waveform. (b) Harmonic spectrum.

three machines. It can be seen that no matter for the proposed 18-slot/8-pole FCFMPM or the comparative PMSMs, the air-gap flux density consists of a series of harmonics, in which the harmonics with the pole pairs of $(N_{\rm st} - p_r)$ and $(N_{\rm st} + p_r)$ are distinct, which is consistent with the conclusion drawn from (10). Moreover, it can be observed from Figs. 7(b) and 8(b) that the amplitude of fundamental component of air-gap flux density in the proposed FCFMPM and the comparative PMSM_1 is almost equal, means that the same fundamental magnetic loading is applied in both machines resulting from the same amount of magnets.

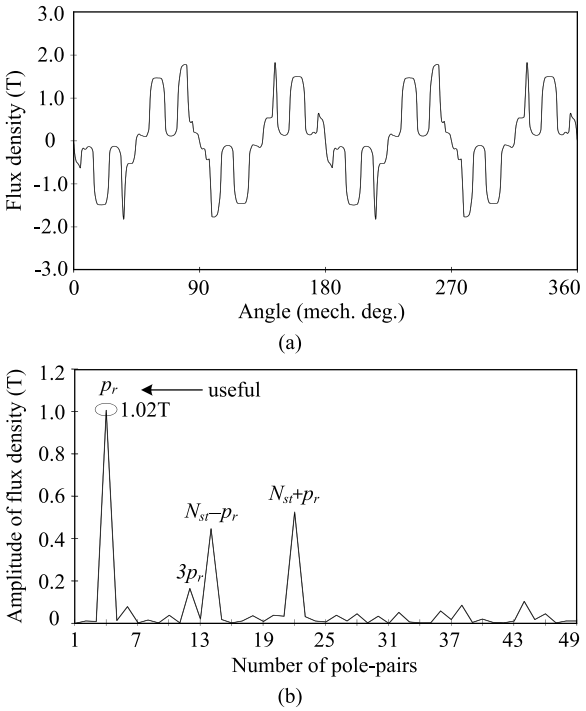

Fig. 8. No-load air-gap flux density of a comparative PMSM_1. (a) Waveform. (b) Harmonic spectrum.

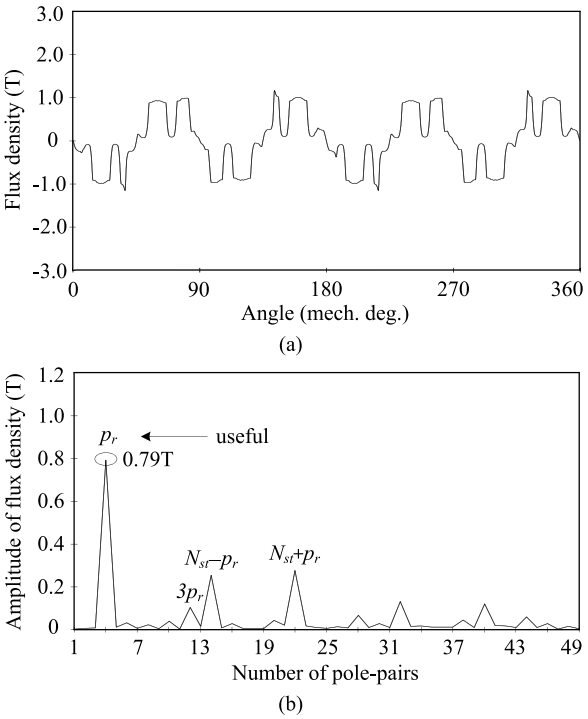

Fig. 9. No-load air-gap flux density of a comparative PMSM_2. (a) Waveform. (b) Harmonic spectrum.

Fig. 9 shows that the air-gap flux density of PMSM_2 is lower than that of PMSM_1 due to reduced length of PMs, which is more advisable in practical applications to be better for improving the magnet material utilization and reducing the iron losses.

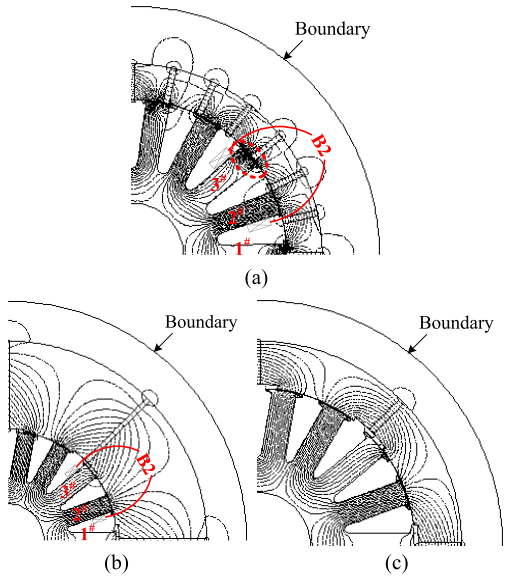

Fig. 10. No-load flux distributions. (a) FCFMPM. (b) PMSM_1. (c) PMSM_2.

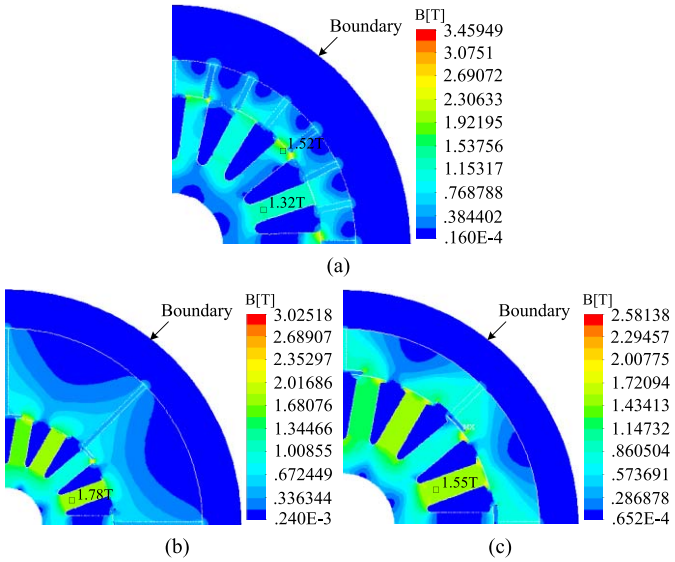

Fig. 11. No-load flux density distributions. (a) FCFMPM. (b) PMSM_1. (c) PMSM_2.

B. Field Distribution

Fig. 10 shows the no-load flux distributions of the proposed 18-slot/8-pole FCFMPM and the comparative PMSMs. It can be seen that although the PM rotor pole pairs in the proposed FCFMPM and the comparative PMSMs are 14 and 4, respectively, their flux distributions on the stator having four pole pairs are the same. Thus, the same winding connection with four pole pairs can be wound in these three machines. Moreover, it can be found that due to the unique field modulation operation, the magnetic flux leakage around the outer surface of the rotor in the FCFMPM machine is more serious than that in the PMSM counterparts. Based on (21), considering the influence of flux leakage effect, the electromagnetic torque of the proposed 18-slot/8-pole FCFMPM should be qualified as

$$T_{\rm ev} = \frac{m I_{\rm ph}}{2}(1-k_{\rm df})k_{d1}N_{\rm ph}L_a r_g(1.97\Lambda_0 F_{\rm ag1} - 3.45\Lambda_1 F_{\rm ag1}) \tag{23}$$

where $k_{\rm df}$ is defined as the flux leakage factor.

Fig. 11 shows the corresponding no-load flux density distributions of these three machines. It can be observed from Fig. 11(a) and (b) that although the same amount of magnets is applied to obtain the same air-gap fundamental magnetic loading, the flux density on stator teeth in the proposed FCFMPM is obviously lower than that in the PMSM_1. Based on Figs. 6 and 10, taking the coil B2 as an example, it can be explained as follows: in the comparative PMSM_1, the air-gap fundamental flux as shaded in Fig. 6(a) can fully link with the coil B2 through $2^{\#}$ and $3^{\#}$ teeth due to the fact that the pole pairs of armature windings are the same as that of PM rotor. However, in the proposed FCFMPM, since the pole pairs of air-gap fundamental flux are G_r times that of the armature windings, only $1/G_r$ of the fundamental flux in one winding pole pitch, as black shaded in Fig. 6(b), can effectively link with the coil B2 through $3^{\#}$ tooth, and other parts close around $3^{\#}$ tooth shoe, as shown in Fig. 10(a) marked by red dotted lines. Thus, the flux density at stator tooth shoes in the FCFMPM is higher than that at stator tooth areas, as shown in Fig. 11(a).

Since the rotor speed is the same but the pole-pairs of PM rotor are different in these two machines, the changing rate of fundamental flux linking armature windings in the proposed FCFMPM is G_r times higher than that in the PMSM_1. Thus, the EMF amplitudes induced by the fundamental flux in both machines are the same, only the electric frequencies of the induced EMF in them are different. Meanwhile, it can be observed that the effective harmonic flux in the proposed FCFMPM, as green shaded in Fig. 6(b), which has a rotational speed of G_r times higher than the rotor and the same pole pairs as the stator windings, can also effectively link with the coil B2 through $2^{\#}$ tooth, thus inducing an additional EMF increment having the same electric frequency with that produced by the fundamental flux.

Fig. 12 shows the on-load flux density distributions of these three machines. Based on Figs. 11 and 12, it can be observed that the effect of armature reaction is weak in the proposed FCFMPM. Compared with the PMSM_1, the stator tooth flux density in the PMSM_2, as shown in Fig. 11(c), is reduced to about 1.5 T due to the decrease of the amount of magnets. Obviously, the on-load flux density distribution of the PMSM_2 is lower than that of the PMSM_1, which is more reasonable in practical machine design. Hence, the performance comparison among the three machines considering the field distribution is more advisable and convincing. Moreover, due to lower stator flux density, the stator yoke in the proposed FCFMPM can be thinner than that in the comparative PMSMs, thus saving iron materials.

C. Cogging Torque

Cogging torque is an important aspect to evaluate the machine performances, which can cause torque ripples and

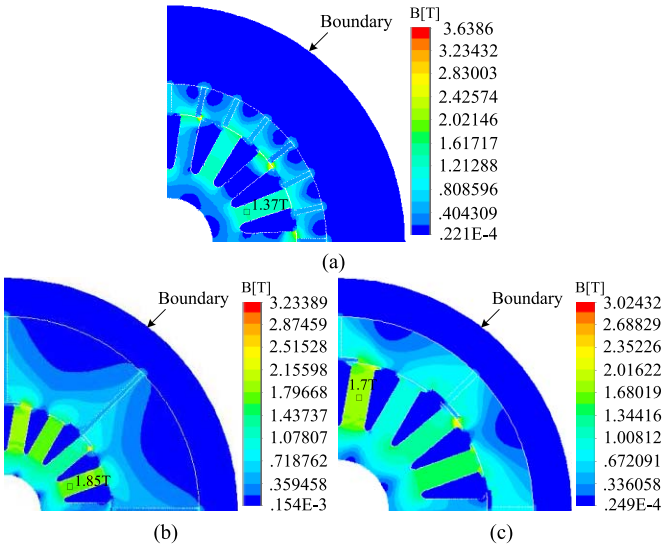

Fig. 12. On-load flux density distributions. (a) FCFMPM. (b) PMSM_1. (c) PMSM_2.

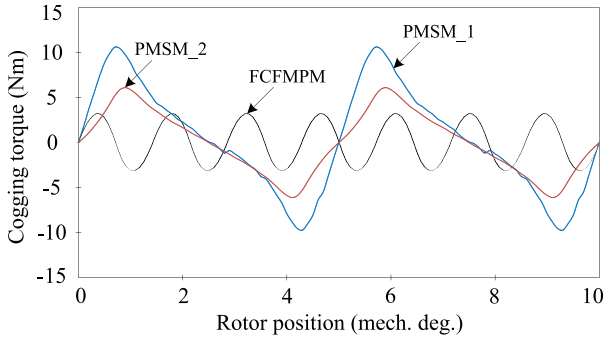

Fig. 13. Cogging torque waveforms.

affect the starting performance. The period of cogging torque of the analyzed machines can be expressed as

$$\delta_{\text{cog}} = \frac{360^\circ}{N_{\text{cog}}} \tag{24}$$

where N_{cog} is the least common multiple between the rotor poles and stator teeth number. For the proposed 18-slot/8-pole FCFMPM, the period of cogging torque in mechanical degree is 1.43°, and it is 5° for the comparative PMSMs.

Fig. 13 shows the cogging torque waveforms of these three machines. It can be seen that the simulated cogging torque periods are consistent with that calculated from (24). It is known that the peak cogging torque can be reduced when a large N_{cog} is adopted. Because the value of N_{cog} of the proposed 18-slot/8-pole FCFMPM is larger than that of the comparative PMSMs, the peak-to-peak cogging torque in the proposed FCFMPM is only 6.1 Nm, which accounts for 2.4% of its transmitted electromagnetic torque. However, the peak-to-peak cogging torque in the comparative PMSM_1 and PMSM_2 are about 20.3 Nm and 12.2 Nm, accounting for 14.9% and 11.7% of their transmitted electromagnetic torques, respectively. The difference of peak-to-peak cogging torque between the PMSM_1 and PMSM_2

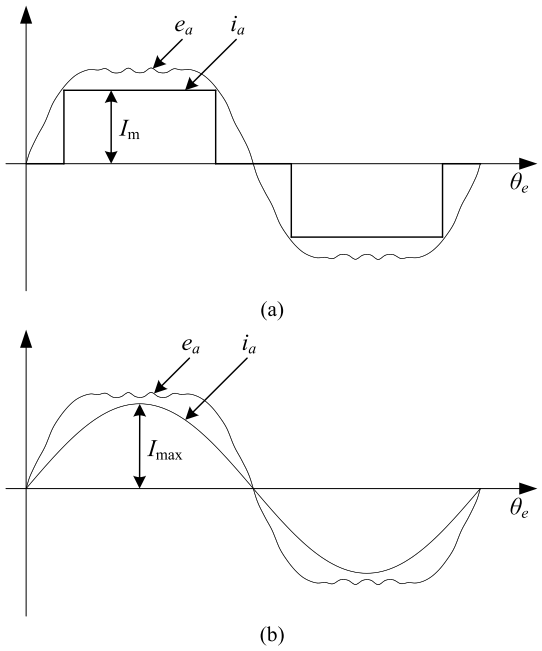

Fig. 14. BLDC and BLAC operation modes for the analyzed PMSMs with trapezoidal back EMF. (a) BLDC operation mode. (b) BLAC operation mode.

is mainly due to the change of applied air-gap magnetic loading.

D. Electromagnetic Torque

As well known, the brushless ac (BLAC) operation is suitable for the machine having a sinusoidal back EMF waveform such as the proposed 18-slot/8-pole FCFMPM, while the brushless dc (BLDC) operation is often adopted in the machine possessing a square-wave back EMF. Because the comparative PMSMs have trapezoidal back EMF, the electromagnetic torque characteristics of these two PMSMs operating at both BLAC and BLDC modes, as shown in Fig. 14, will be discussed.

Fig. 14(a) shows the BLDC operation with 120° conduction mode. Fig. 14(b) shows the BLAC operation in which $i_d = 0$ control method is adopted, namely, applying the armature current in phase with the back EMF. In addition, the applied RMS current under the BLDC and BLAC operation modes in three machines is the same. It is governed by

$$I_m = \frac{\sqrt{3}}{2} I_{\text{max}} \tag{25}$$

where I_m is the applied dc current in BLDC operation mode, as shown in Fig. 14(a), and I_{max} is the peak value of applied ac current in BLAC operation mode, as shown in Fig. 14(b).

Fig. 15 shows the electromagnetic torque waveforms of these three machines under BLDC and BLAC operation modes calculated using FEA. The corresponding torque parameters are listed in Table II, where T_{e_max}, T_{e_min}, T_{e_rip}, and T_{e_avg} are the maximum, minimum, ripple, and average torques, respectively.

It can be found that the average torque T_{e_avg} of the PMSM_1 and PMSM_2 under BLAC operation is slightly

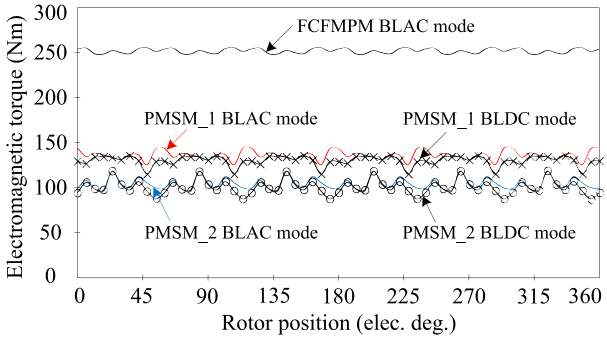

Fig. 15. Electromagnetic torque waveforms of these three machines under BLDC and BLAC operation modes.

TABLE II
COMPARISON OF THE ELECTROMAGNETIC TORQUE CAPABILITIES

	BLAC mode			BLDC mode	
	FCFMPM	PMSM_1	PMSM_2	PMSM_1	PMSM_2
T_{e_max} (Nm)	255.1	144.0	117.6	135.3	118.3
T_{e_min} (Nm)	248.5	125.4	95.8	115.0	87.7
T_{e_rip} (Nm)	6.6	18.6	21.8	20.3	30.6
T_{e_avg} (Nm)	251.8	136.1	103.9	129.8	100.6

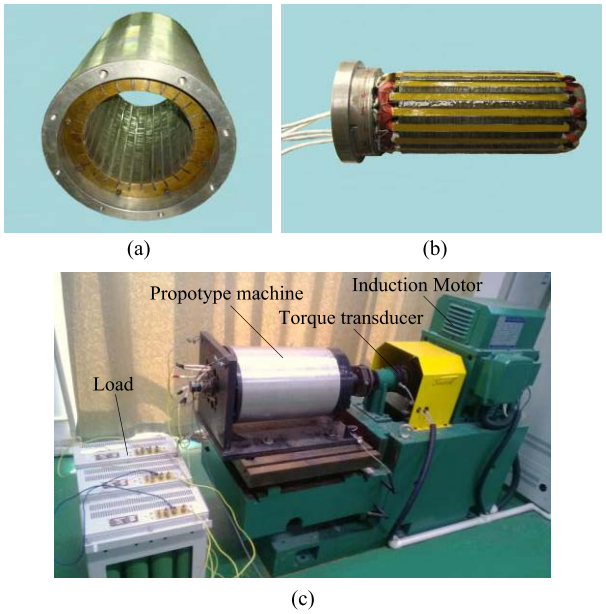

Fig. 16. Prototype machine setup. (a) Outer rotor. (b) Stator. (c) Test bed.

bigger than that under BLDC operation, while their corresponding ripple torque T_{e_rip} under BLAC operation reduces by 8.4% and 28.8%, as compared with the BLDC operation, respectively. That is, the BLAC operation is more suitable for the comparative PMSMs. On the other hand, under BLAC operation, the torque ripple T_{e_rip} of the proposed 18-slot/8-pole FCFMPM machine is only 35.5% and 30.3% of that of the comparative PMSM_1 and PMSM_2, and the offered average torque T_{e_avg} is about 1.85 times and 2.4 times larger than that of the PMSM_1 and PMSM_2, respectively. It can be seen that the torque capability comparison between the proposed FCFMPM machine and PMSM counterparts agrees with the theoretical analysis by (22) and (23).

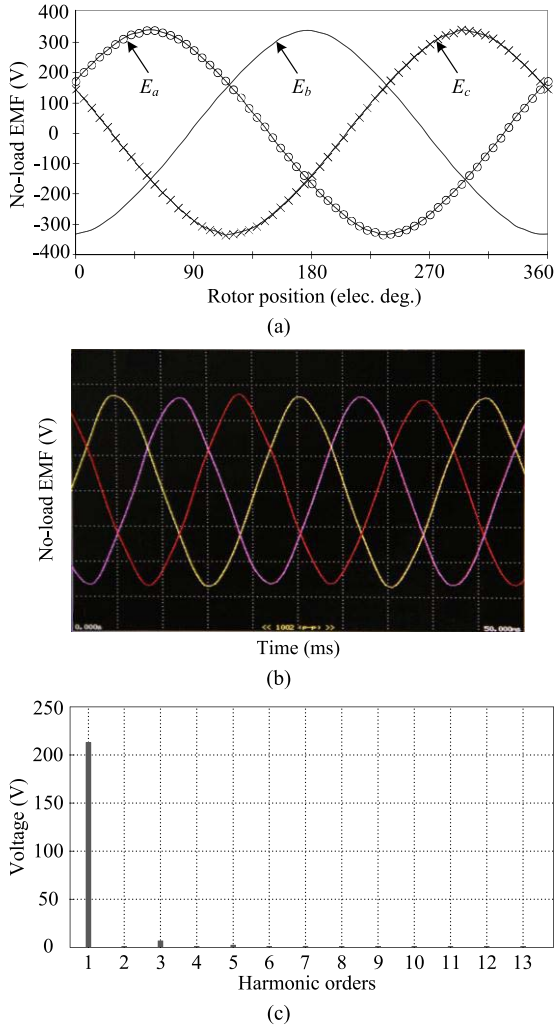

Fig. 17. No-load back EMF at 214 r/min. (a) FEA results. (b) Measured EMF waveforms (120 V/div and 5 ms/div). (c) Harmonics of measured EMF.

Hence, the FEA results confirm that the proposed FCFMPM can offer higher torque capability than the PMSM counterparts.

V. EXPERIMENTAL VERIFICATION

As shown in Fig. 16, an 18-slot/8-pole FCFMPM prototype machine has been built for experimentation to verify the validity. The detailed specifications and key design parameters of the prototype are the same as those listed in Table I.

The measured three-phase no-load back EMF waveforms are given in Fig. 17(b) as well as compared with the 2-D FEA results, as shown in Fig. 17(a). It can be found that the measured EMF waveforms have a good agreement with FEA results. Fig. 17(c) shows the harmonic components of the measured EMF. It can be calculated from Fig. 17(c) that the total harmonic distortion of the measured EMF is about 2.94%. Moreover, the fundamental RMS value of the measured EMF is about 214 V, which is reduced by 6.14% compared with the FEA results. It is mainly due to the manufacturing imperfection and the unaccounted flux leakage at the end regions in the 2-D FEA.

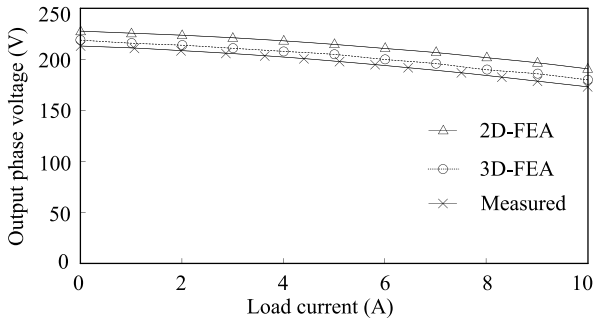

Fig. 18. Simulated and measured output voltage versus load current of the prototype machine at 214 r/min.

TABLE III
COMPARISON BETWEEN THE SIMULATED AND MEASURED OUTPUT VOLTAGES

	2D-FEA	3D-FEA	Measured
No-load EMF (V)	228	219	214
Output voltage at rated current (V)	200	189	181
Voltage regulation	12.3%	13.7%	15.4%

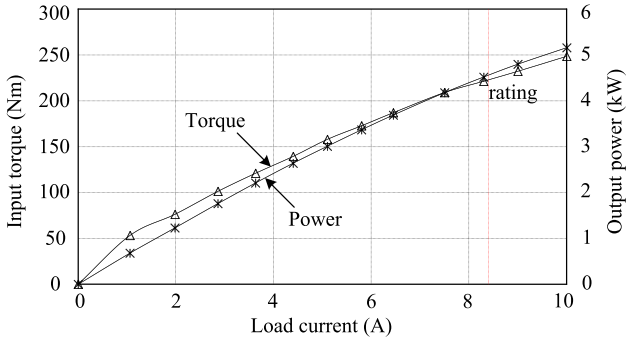

Fig. 19. Measured input torque and output power versus load current of the prototype machine at 214 r/min.

As shown in Fig. 16(c), the prototype machine is operated as a generator driven by an induction motor, and Y-connected symmetrical three-phase resistances are applied as the load for experiments to assess output characteristics of the prototype machine. Fig. 18 shows the measured output voltage versus the load current under the rated speed 214 r/min as well as compared with the FEA results. It can be seen that the measured results have the same changing trend with the FEA. But there is some discrepancy between the 2-D FEA and measured results. Thus, the 3-D FEA is performed and also shown in Fig. 18, and the comparison of the results between them is listed in Table III. It can be seen that the output voltage is reduced by about 5% due to the end effects. In addition, the error between the 3-D FEA and measured results are mainly caused by the manufacturing imperfection. The measured voltage regulation at the rated current is about 15.4%, means that there is a low voltage drop on the internal impedance of the FCFMPM prototype machine.

As shown in Fig. 16(c), a torque transducer is used to measure input torque of the prototype machine in the experiments. Fig. 19 shows the variations of the measured input torque and output power with the load currents when the rotor speed is kept at 214 r/min. It can be seen that when the rated current 8.33 A is achieved, the prototype output power is about 4.5 kW, and the measured input torque is about 221 Nm, which is consistent with the FEA results by considering the influence of fabrication errors and 2-D FEA end-effects. Thus, the measured torque capability of the prototype machine is up to 20.5 kNm/m^3 under the naturally cooled condition. Moreover, it can be calculated that the measured efficiency under rated conditions is about 0.91.

VI. CONCLUSION

In this paper, a FCFMPM machine, which is particularly attractive for direct drive applications, has been presented, analyzed, compared, and implemented. The operating principle analysis including theoretically deriving the air-gap flux density, no-load EMF, and electromagnetic torque expressions has revealed that adding to the air-gap fundamental flux, the utilization of effective harmonic flux makes the proposed FCFMPM machine to offer higher torque capability compared with the PMSM counterparts. Using the FEA, the performances comparison between them has identified the advantage of high torque capability of the proposed FCFMPM machine. Although the comparative PMSM counterpart is not fabricated, the experimental tests on an 18-slot/8-pole FCFMPM prototype machine have been conducted to verify the validity of FEA results, sufficiently illustrating that the proposed FCFMPM machine possesses better performances than the PMSM counterparts especially in aspects of high torque capability.

ACKNOWLEDGMENT

This work was supported in part by the 973 Program of China under Project 2013CB035603, and in part by the National Natural Science Foundation of China under Project 51137001.

REFERENCES

[1] M. Cheng and Y. Zhu, "The state of the art of wind energy conversion systems and technologies: A review," *Energy Convers. Manage.*, vol. 88, pp. 332–347, Dec. 2014.
[2] M. Cheng and C. C. Chan, "General requirement of traction motor drives," in *Encyclopedia of Automotive Engineering*, D. Crolla, D. E. Foster, T. Kobayashi, and N. Vaughan, Eds. New York, NY, USA: Wiley, 2014.
[3] K. T. Chau, C. C. Chan, and C. Liu, "Overview of permanent-magnet brushless drives for electric and hybrid electric vehicles," *IEEE Trans. Ind. Electron.*, vol. 55, no. 6, pp. 2246–2257, Jun. 2008.
[4] D. McMillan and G. W. Ault, "Techno-economic comparison of operational aspects for direct drive and gearbox-driven wind turbines," *IEEE Trans. Energy Convers.*, vol. 25, no. 1, pp. 191–198, Mar. 2010.
[5] J. Y. Chen, C. V. Nayar, and L. Xu, "Design and finite-element analysis of an outer-rotor permanent-magnet generator for directly coupled wind turbines," *IEEE Trans. Magn.*, vol. 36, no. 5, pp. 3802–3809, Sep. 2000.
[6] W. Fei and P. C.-K. Luk, "Torque ripple reduction of a direct-drive permanent-magnet synchronous machine by material-efficient axial pole pairing," *IEEE Trans. Ind. Electron.*, vol. 59, no. 6, pp. 2601–2611, Jun. 2012.
[7] M. Pinilla, "Performance improvement in a renewable energy direct drive permanent magnet machine by means of soft magnetic composite interpoles," *IEEE Trans. Energy Convers.*, vol. 27, no. 2, pp. 440–448, Jun. 2012.

[8] L. Xu, "Dual-mechanical-port electric machines-concept and application of a new electric," *IEEE Ind. Appl. Mag.*, vol. 15, no. 4, pp. 44–51, Jul./Aug. 2009.
[9] X. Sun, M. Cheng, Y. Zhu, and L. Xu, "Application of electrical variable transmission in wind power generation system," *IEEE Trans. Ind. Appl.*, vol. 49, no. 3, pp. 1299–1307, May/Jun. 2013.
[10] K. Atallah and D. Howe, "A novel high-performance magnetic gear," *IEEE Trans. Magn.*, vol. 37, no. 4, pp. 2844–2846, Jul. 2001.
[11] L. Jian, K. T. Chau, Y. Gong, J. Z. Jiang, C. Yu, and W. Li, "Comparison of coaxial magnetic gears with different topologies," *IEEE Trans. Magn.*, vol. 45, no. 10, pp. 4526–4529, Oct. 2009.
[12] A. Toba and T. A. Lipo, "Generic torque-maximizing design methodology of surface permanent-magnet vernier machine," *IEEE Trans. Ind. Appl.*, vol. 36, no. 6, pp. 1539–1546, Nov./Dec. 2000.
[13] D. Li, R. Qu, and T. Lipo, "High power factor vernier permanent magnet machines," in *Proc. IEEE ECCE*, Sep. 2013, pp. 1534–1540.
[14] L. Jian, K. T. Chau, and J. Z. Jiang, "A magnetic-geared outer-rotor permanent-magnet brushless machine for wind power generation," *IEEE Trans. Ind. Appl.*, vol. 45, no. 3, pp. 954–962, May/Jun. 2009.
[15] K. T. Chau, D. Zhang, J. Z. Jiang, C. Liu, and Y. Zhang, "Design of a magnetic-geared outer-rotor permanent-magnet brushless motor for electric vehicles," *IEEE Trans. Magn.*, vol. 43, no. 6, pp. 2504–2506, Jun. 2007.
[16] L. L. Wang, J. X. Shen, P. C. K. Luk, W. Z. Fei, C. F. Wang, and H. Hao, "Development of a magnetic-geared permanent-magnet brushless motor," *IEEE Trans. Magn.*, vol. 45, no. 10, pp. 4578–4581, Oct. 2009.
[17] J. Li, K. T. Chau, J. Z. Jiang, C. Liu, and W. Li, "A new efficient permanent-magnet vernier machine for wind power generation," *IEEE Trans. Magn.*, vol. 46, no. 6, pp. 1475–1478, Jun. 2010.
[18] X. Li, K. T. Chau, M. Cheng, and W. Hua, "Comparison of magnetic-geared permanent-magnet machines," *Prog. Electromagn. Res.*, vol. 133, pp. 177–198, Jan. 2013.
[19] R. Hosoya, H. Shimada, and S. Shimomura, "Design of a ferrite magnet vernier machine for an in-wheel machine," in *Proc. IEEE ECCE*, Sep. 2011, pp. 2790–2797.
[20] C. Liu, J. Zhong, and K. T. Chau, "A novel flux-controllable vernier permanent-magnet machine," *IEEE Trans. Magn.*, vol. 47, no. 10, pp. 4238–4241, Oct. 2011.
[21] S. L. Ho, S. Niu, and W. N. Fu, "Design and comparison of vernier permanent magnet machines," *IEEE Trans. Magn.*, vol. 47, no. 10, pp. 3280–3283, Oct. 2011.
[22] S. Niu, S. L. Ho, W. N. Fu, and L. L. Wang, "Quantitative comparison of novel vernier permanent magnet machines," *IEEE Trans. Magn.*, vol. 46, no. 6, pp. 2032–2035, Jun. 2010.
[23] X. Li, K. T. Chau, and M. Cheng, "Analysis, design and experimental verification of a field-modulated permanent-magnet machine for direct-drive wind turbines," *IET Electr. Power Appl.*, vol. 9, no. 2, pp. 150–159, Feb. 2015.

Xianglin Li was born in Shandong, China, in 1984. He received the B.S. and M.S. degrees from the College of Information and Control Engineering, China University of Petroleum, Qingdao, China, in 2007 and 2010, respectively. He is currently pursuing the Ph.D. degree in electrical engineering with Southeast University, Nanjing, China.

He was a Visiting Student funded by the China Scholarship Council with the Wisconsin Electric Machines and Power Electronics Consortium Program, Department of Mechanical Engineering, University of Wisconsin—Madison, Madison, WI, USA, from 2012 to 2013, where he did research on the analysis and design of permanent-magnet vernier machine. Since 2014, he has been a Research Assistant with the Department of Electrical and Electronic Engineering, University of Hong Kong, Hong Kong. His current research interests include analysis, design, and control of permanent-magnet machines.

Kwok tong Chau (M'89–SM'04–F'13) received the B.Sc. (Eng.) (Hons.), M.Phil., and Ph.D. degrees in electrical and electronic engineering from the University of Hong Kong, Hong Kong, in 1988, 1991, and 1993, respectively.

He is currently a Full Professor with the Department of Electrical and Electronic Engineering, University of Hong Kong, where he is also the Director of the International Research Center for Electric Vehicles. He has authored four books, seven book chapters, and over 180 refereed journal papers. His current research interests include electric and hybrid vehicles, machine and drives, and clean energy.

Ming Cheng (F'15) received the B.Sc. and M.Sc. degrees from the Department of Electrical Engineering, Southeast University, Nanjing, China, in 1982 and 1987, respectively, and the Ph.D. degree from the Department of Electrical and Electronic Engineering, University of Hong Kong, Hong Kong, in 2001.

He was a Visiting Professor with the Wisconsin Electric Machines and Power Electronics Consortium, University of Wisconsin—Madison, Madison, WI, USA, in 2011, and the Department of Energy Technology, Aalborg University, Aalborg, Denmark, in 2012. Since 1987, he has been with Southeast University, where he is currently a Professor with the School of Electrical Engineering, the Director of the Research Center for Wind Power Generation, and the Co-Director of the Yancheng Institute of New Energy Vehicles. He has authored over 250 technical papers and four books, and holds over 50 patents in these areas. His current research interests include electrical machines, motor drives for electric vehicles, and renewable energy generation.

Byungtaek Kim (M'01) was born in Seoul, Korea. He received the B.S., M.S., and Ph.D. degrees in electrical engineering from Hanyang University, Seoul, Korea, in 1994, 1996, and 2001, respectively.

He was with Samsung Electro-Mechanics Inc., Suwon, Korea, for seven years, and LG Electronics Inc., Seoul, for three years. He became a Professor of Electrical Engineering with Kunsan National University, Gunsan, Korea, in 2005. In 2012, he was a Visiting Scholar with the Department of Electrical and Computer Engineering, University of Wisconsin—Madison, Madison, WI, USA. His current research interests include electric machines and power electronics.

Robert D. Lorenz (F'98) received the B.S., M.S., and Ph.D. degrees from the University of Wisconsin—Madison, Madison, WI, USA.

He has been a faculty member with the University of Wisconsin—Madison, since 1984, where he is currently the Co-Director of the Wisconsin Electric Machines and Power Electronics Consortium. He is engaged in fundamental and applied research in control of electromagnetic actuators and power electronics, identifying and controlling nonlinear electro-mechanics, and power electronics in industrial, aerospace, and office automation systems. He has authored over 300 papers concerned with the related topic in IEEE journals and academic conferences.

Dr. Lorenz was a recipient of the 26 prestigious awards granted by the IEEE, including the Power Electronics and Motion Control Conference Outstanding Achievement Award in 2006, the Industry Applications Society (IAS) Distinguished Service Award in 2011, and the IEEE Kaufman Award by the IEEE IAS in 2013. He was a Distinguished Lecturer of the IEEE IAS in 2000/2001 and the President of the IEEE IAS in 2001.